Surface second-harmonic generation from scattering of surface plasmon polaritons from radially symmetric nanostructures

Lina Cao*
Department of Chemistry, Columbia University, New York, New York 10027, USA

N. C. Panoiu
Department of Electronic and Electrical Engineering, Photonics Group, University College London, Torrington Place, London WC1E 7JE, United Kingdom

Ravi D. R. Bhat and R. M. Osgood, Jr.
Department of Applied Physics and Applied Mathematics, Columbia University, New York, New York 10027, USA
(Received 6 February 2009; revised manuscript received 1 May 2009; published 16 June 2009)

We present a comprehensive study of linear and nonlinear effects observed in the scattering process of surface plasmon polaritons (SPPs) from localized two-dimensional surface deformations at a metal/dielectric interface. Thus, the electromagnetic field at the fundamental frequency (FF), for both *p* and *s* polarizations, is first determined by solving the corresponding set of reduced Rayleigh equations. The complete solution of these equations allows us to investigate both the complex structure of the scattered electromagnetic field as well as subtle mechanisms by which incident SPPs are scattered into radiative modes (light) and outgoing SPP waves. Furthermore, the electromagnetic field at the FF is used to determine the nonlinear surface polarization at the second harmonic (SH) and subsequently both the electromagnetic field distributions as well as the amount of light generated at the SH. Calculations are performed for three geometries that are relevant in many experiments, namely, Gaussian, hemispherical, and cylindrical nanodefects. Finally, throughout our analysis, we discuss potential applications of our findings to surface spectroscopy, surface chemistry, or imaging techniques of surface nanodefects.

DOI: 10.1103/PhysRevB.79.235416 PACS number(s): 73.20.Mf, 78.67.−n, 41.20.Jb

I. INTRODUCTION

Over the last few years, we have witnessed a renewed interest in both the physical properties of surface plasmon polaritons (SPPs) as well as their use in nanodevices with new or improved functionality. In particular, recent advances in materials, surface science, and nanofabrication techniques have made possible the design and experimental implementation of new plasmonic nanostructures and nanodevices, which exhibit remarkable physical properties and a great potential for advanced technological applications. To this end, of particular interest has been the optical properties of SPPs, which are strongly localized *p*-polarized surfaced waves formed at the interface between a metal and a dielectric,[1–4] as well as their interaction with metallic nanostructures.[5–7] One of the consequences of the extreme light localization at metal/dielectric interfaces or close to the surface of metallic nanoparticles is that extended (propagating waves) or localized surface plasmon polaritons can be used to achieve strong enhancement of the electromagnetic field, a property with important technological applications. To be more specific, this property can be employed to design new linear plasmonic devices,[8–16] detectors, and other photovoltaic devices (solar cells),[17–20] optical sensors,[21,22] or study a series of photochemical processes.[23,24] In addition, and also of particular importance for practical applications, the strong enhancement of the electromagnetic field leads to the possibility to achieve strong nonlinear optical effects, such as second harmonic (SH) generation (SHG) (Refs. 1–7 and 25–35) and surface-enhanced Raman scattering (SERS),[36–39] at remarkably low optical power.

Surface SHG has become an essential diagnostic tool for physical chemistry, noninvasive surface analysis, and catalytic chemistry, chiefly because this nonlinear optical wave interaction is strongly dependent on the physical properties and local structure of surfaces and interfaces. This sensitivity of SHG is particularly important if one considers SHG at the surface of a centrosymmetric material, as in this case the lack of dipole-allowed optical transitions in the bulk of such materials leads to the vanishing of the otherwise dominant bulk SHG. In this case, the total SH signal is generated within a layer of only a few angstroms thickness, and therefore it is strongly dependent on the physical structure of this surface layer or its chemical properties, e.g., the nature of adsorbates at the surface or interface. In addition, surface SHG is a useful probing technique because it is noninvasive and has micrometer-scale spatial resolution. Moreover, the properties of surface SHG process, e.g., the polarization of the generated signal and the spatial distribution of the near and far fields, are markedly different from those of the corresponding linear scattering process and further enabling this nonlinear optical process to be a unique tool for the analysis of surfaces and interfaces.

In the standard approach to nonlinear surface probing, a laser source illuminates a surface and the scattered radiation is detected. In some cases metal particles are present on the surface and in that case it is well known that the scattering process is enhanced via the excitation of local surface-plasmon-polariton modes in the metal object. More recently the interest in propagating plasmon polaritons has led several groups to consider the use of these waves as the primary

probing source of surface features. Indeed recent beautiful work involving photoemission electron microscopy studies of illuminated surfaces[40] has shown that this approach is not only useful but can also provide a route to examine coherent plasmon effects. The question then arises as to whether this "plasmon-source" approach could also provide a useful source to examine surface features via nonlinear surface wave excitation. Such an approach would have the advantage of a closer coupling of the excitation source with the surface feature to be examined. Further it would also be possible to envision using nonoptical excitation means such as injected electrons.

Thus, in this paper we examine the physics of two-dimensional (2D) wave scattering from surface nanodefects. In fact we extend our earlier analysis[32] of the SHG from scattering of SPP waves from one-dimensional (1D) surface nanodefects to the more realistic case of two-dimensional radially symmetric surface nanodefects. Importantly, our analysis does not simply extends the results obtained in the 1D case to the 2D geometry, as the latter case presents an additional complexity that stems from the more intricate polarization properties of the electromagnetic field that is generated near a 2D metallic nanodefect. Thus, unlike the 1D case, when both the SPP waves and the radiated light are *p* polarized, in the 2D case the radiative modes have both *s*- and *p*-polarized components. This increased degree of complexity has important implications for the structure of the near- and far-field angular distributions and the magnitude of emitted radiation, both at the fundamental frequency (FF) and at the SH.

The paper is organized as follows. In Sec. II, we introduce the analytical formulation of our problem and the numerical method we used in our approach. Thus, we introduce a set of coupled-reduced Rayleigh equations whose solution fully determines the electromagnetic field at the FF. Also, we introduce the numerical method used to solve this system of equations. Moreover, we describe our approach to determine the electromagnetic field and the amount of emitted radiation at the SH from the electromagnetic field at the FF. In Sec. III, we present our results obtained by solving this analytical model. Thus, we consider three different radially symmetric surface nanodefects, namely, Gaussian, hemispherical, and cylindrical nanodefects, and for each of them we determine the spectral properties and the spatial distribution of the field at the FF and SH. Also, we investigate the influence of the geometrical structure of the nanodefect on the scattering process. In the last section, we summarize our results.

II. THEORETICAL APPROACH AND NUMERICAL ALGORITHM

In this section we present the theoretical formalism used to analyze the scattering of SPPs from surface metallic nanodefects as well as the numerical method used in our analysis. Our calculations provide the spatial distribution of the electromagnetic field and the spatial pattern of the radiated light, both at the FF and the SH.

A. Linear scattering of surface plasmon polaritons

In order to study the scattering process of SPP waves from surface nanodefects, we consider a system consisting of a

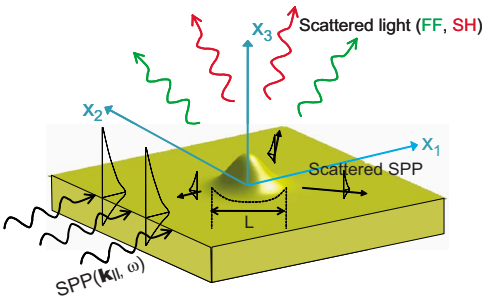

FIG. 1. (Color online) Schematic of the scattering geometry and the radiated waves involved in the nonlinear scattering process. Fields in the region denoted by $L=3.5R$ are integrated to calculate SHG.

SPP wave propagating on a planar metallic surface located in the (x_1,x_2) plane, a wave that is incident onto a surface nanodefect; the corresponding geometry is illustrated in Fig. 1. The surface profile, which for the sake of simplicity is chosen to be radially symmetric, is described by a surface-profile function $x_3=\zeta(x_\parallel)$, where $\mathbf{x}_\parallel \equiv (x_1,x_2)$. For the function $\zeta(\mathbf{x}_\parallel)$, which describes the shape of the surface nanodefect, we considered three choices, namely, a Gaussian, $\zeta(\mathbf{x}_\parallel)=h \times \exp(-x_\parallel^2/R^2)$, with height h and width R; a cylinder, $\zeta(\mathbf{x}_\parallel)=h, x_\parallel \leq R$, with height h and radius R; and a spherical cap, $\zeta(\mathbf{x}_\parallel)=\pm(\sqrt{R^2-x_\parallel^2}-\sqrt{R^2-\varrho^2}), x_\parallel \leq \varrho$, with R and ϱ as the radius of the sphere and the cap, respectively. Note that with these choices for the surface-profile function $\zeta(\mathbf{x}_\parallel)$ we can study surfaces with both protuberances $(h>0)$ and indentations $(h<0)$. The incoming SPP propagates along the x_1 direction and, upon its interaction with the surface nanodefect, generates scattered SPP waves as well as radiative modes (photon states), which propagate outwardly, away from the nanodefect.

We consider that the SPP propagates at the interface between vacuum and a metal, which is chosen to be silver in our calculations; the extension to the more general case of a dielectric/metal interface is trivial. The electromagnetic properties of the metal are modeled via a dielectric function that obeys the Drude model, $\epsilon(\omega)=1-\omega_p^2/\omega^2$, where ω_p is the plasma frequency of the metal and ω is the frequency. For silver, the corresponding plasma wavelength is $\lambda_p = 145.9$ nm.[41] Note that this choice for the metal dielectric function does not take into account the optical losses, that is, the imaginary part of $\epsilon(\omega)$ is set to zero; however, this is a good approximation since the characteristic size of the nanodefect is much smaller than the plasmon absorption length, and therefore only a negligible amount of energy is dissipated during the scattering process. As a result, the electromagnetic energy is conserved during the scattering process. Accounting for loss is relatively straightforward since its effect on the wave is over a scale size which is much longer than that of the scatterer.

In order to analyze the scattering process of the SPP wave at the FF, we employ a method based upon a set of coupled-reduced Rayleigh equations.[2,42–44] To begin with, it is assumed that in the vacuum region, $x_3>\zeta(x_\parallel)$, the amplitude $\mathbf{E}(\mathbf{x};\omega)$ of the electric field, which is defined by the harmonic dependence $\mathbf{E}(\mathbf{x};t)=\mathbf{E}(\mathbf{x};\omega)e^{i\omega t}$, consists of the inci-

dent SPP wave and a scattered field that contains both radiative modes (scattered light) and scattered SPP waves:

$$\mathbf{E}^{\uparrow}(\mathbf{x};\omega) = \frac{c}{\omega}[i\hat{\mathbf{x}}_1\beta_0(\omega) - \hat{\mathbf{x}}_3 k_{\parallel}(\omega)]e^{ik_{\parallel}(\omega)x_1 - \beta_0(\omega)x_3} + \int \frac{d^2\mathbf{q}_{\parallel}}{(2\pi)^2}\left\{\frac{c}{\omega}[i\mathbf{q}_{\parallel}\alpha_0(q_{\parallel}) - \hat{\mathbf{x}}_3 q_{\parallel}]A_p(\mathbf{q}_{\parallel}) + (\hat{\mathbf{x}}_3 \times \mathbf{q}_{\parallel})A_s(\mathbf{q}_{\parallel})\right\}e^{i\mathbf{q}_{\parallel}\cdot\mathbf{x}_{\parallel} - \alpha_0(q_{\parallel})x_3}. \quad (1)$$

Here, $\mathbf{E}^{\uparrow}(\mathbf{x};\omega)$ is the electric field at the frequency ω, the arrow designates the vacuum region, $k_{\parallel}(\omega)$ and $\beta_0(\omega)$ are the plasmon wave vector and the inverse decay length of the field in the direction normal to the surface, respectively, and are given by the relations

$$k_{\parallel}(\omega) = \frac{\omega}{c}\sqrt{\frac{\epsilon(\omega)}{\epsilon(\omega)+1}}, \quad (2a)$$

$$\beta_0(\omega) = \frac{\omega}{c}\sqrt{\frac{-1}{\epsilon(\omega)+1}}. \quad (2b)$$

These components of the plasmon wave vector satisfy the dispersion relation $k_{\parallel}^2(\omega) - \beta_0^2(\omega) = \frac{\omega^2}{c^2}$. Moreover, the function $\alpha_0(q_{\parallel})$ is defined by

$$\alpha_0(q_{\parallel}) = \begin{cases} \sqrt{q_{\parallel}^2 - \dfrac{\omega^2}{c^2}}, & q_{\parallel} > \dfrac{\omega}{c} \\ -i\sqrt{\dfrac{\omega^2}{c^2} - q_{\parallel}^2}, & q_{\parallel} < \dfrac{\omega}{c}, \end{cases} \quad (3)$$

where the vector $\mathbf{q}_{\parallel} = (q_1, q_2, 0)$ is parallel to the metal surface. Note that for a surface plasmon $k_{\parallel}(\omega) > \omega/c$, and therefore $\alpha_0[k_{\parallel}(\omega)] = \beta_0(\omega)$. Finally, $A_s(\mathbf{q}_{\parallel})$ and $A_p(\mathbf{q}_{\parallel})$ are scattering amplitudes of the s- and p-polarized waves, respectively. Based on the definition of $\alpha_0(q_{\parallel})$ [Eq. (3)], it can be seen that for $q_{\parallel} > \frac{\omega}{c}$ the scattered waves in Eq. (1) are evanescent waves, whereas for $q_{\parallel} < \frac{\omega}{c}$ they are electromagnetic plane waves (radiative modes) scattered into the vacuum. Note that the expansion given in Eq. (1) is valid within the Rayleigh hypothesis, namely, close to the surface the series expansion of the electromagnetic field contains only outward propagating waves. In particular, for small surface nanodefects this assumption is rigorously satisfied.[45]

In order to calculate the scattering amplitudes $A_s(\mathbf{q}_{\parallel})$ and $A_p(\mathbf{q}_{\parallel})$, one requires that Eq. (1) together with the corresponding equation for the metal region satisfy the boundary conditions at the vacuum/metal interface, a condition that can be cast into a set of coupled-reduced Rayleigh equations:[42,46]

$$f_i(p_{\parallel})A_i(\mathbf{p}_{\parallel}) + \sum_{j=s,p}\int \frac{d^2\mathbf{q}_{\parallel}}{(2\pi)^2} g_{ij}(\mathbf{p}_{\parallel},\mathbf{q}_{\parallel})A_j(\mathbf{q}_{\parallel}) = -g_{ip}(\mathbf{p}_{\parallel},\mathbf{k}_{\parallel}), \quad i = p,s \quad (4)$$

where the functions $f_{s,p}$ are given by

$$f_s(p_{\parallel}) = \frac{\alpha_0(p_{\parallel}) + \alpha(p_{\parallel})}{1 - \epsilon(\omega)}, \quad (5a)$$

$$f_p(p_{\parallel}) = \frac{\epsilon(\omega)\alpha_0(p_{\parallel}) + \alpha(p_{\parallel})}{1 - \epsilon(\omega)}, \quad (5b)$$

with

$$\alpha(q_{\parallel}) = \sqrt{q_{\parallel}^2 - \epsilon(\omega)\frac{\omega^2}{c^2}} \quad (6)$$

being the inverse decay length of the electromagnetic field inside the metal. The kernel functions g_{ij} are given by the following expressions:

$$g_{ss}(\mathbf{p}_{\parallel},\mathbf{q}_{\parallel}) = J(\mathbf{p}_{\parallel},\mathbf{q}_{\parallel})\frac{\omega^2}{c^2}\hat{\mathbf{p}}_{\parallel}\cdot\hat{\mathbf{q}}_{\parallel}, \quad (7a)$$

$$g_{pp}(\mathbf{p}_{\parallel},\mathbf{q}_{\parallel}) = J(\mathbf{p}_{\parallel},\mathbf{q}_{\parallel})[p_{\parallel}q_{\parallel} - \alpha(p_{\parallel})\alpha_0(q_{\parallel})\hat{\mathbf{p}}_{\parallel}\cdot\hat{\mathbf{q}}_{\parallel}], \quad (7b)$$

$$g_{sp}(\mathbf{p}_{\parallel},\mathbf{q}_{\parallel}) = iJ(\mathbf{p}_{\parallel},\mathbf{q}_{\parallel})\frac{\omega}{c}\alpha_0(q_{\parallel})(\hat{\mathbf{p}}_{\parallel}\times\hat{\mathbf{q}}_{\parallel})_3, \quad (7c)$$

$$g_{ps}(\mathbf{p}_{\parallel},\mathbf{q}_{\parallel}) = -iJ(\mathbf{p}_{\parallel},\mathbf{q}_{\parallel})\frac{\omega}{c}\alpha(p_{\parallel})(\hat{\mathbf{p}}_{\parallel}\times\hat{\mathbf{q}}_{\parallel})_3. \quad (7d)$$

Here, $\hat{\mathbf{p}}_{\parallel}$ and $\hat{\mathbf{q}}_{\parallel}$ are unit vectors and the function $J(\mathbf{p}_{\parallel},\mathbf{q}_{\parallel})$ is defined as

$$J(\mathbf{p}_{\parallel},\mathbf{q}_{\parallel}) = \int d^2\mathbf{x}_{\parallel}\frac{e^{[\alpha(p_{\parallel})-\alpha_0(p_{\parallel})]\zeta(\mathbf{x}_{\parallel})} - 1}{\alpha(q_{\parallel}) - \alpha_0(q_{\parallel})}e^{i(\mathbf{q}_{\parallel}-\mathbf{p}_{\parallel})\cdot\mathbf{x}_{\parallel}} \quad (8)$$

We now introduce the azimuthal angles ϕ_x, ϕ_q, and ϕ_p, which characterize the direction of the vectors $\mathbf{x}_{\parallel}$, $\mathbf{q}_{\parallel}$, and $\mathbf{p}_{\parallel}$, respectively. The scattering amplitudes $A_s(\mathbf{q}_{\parallel})$ and $A_p(\mathbf{q}_{\parallel})$ are then expanded in Fourier series,

$$A_j(\mathbf{q}_{\parallel}) = \sum_{n=-\infty}^{\infty} A_j^{(n)}(q_{\parallel})e^{in\phi_q}, \quad j = s,p, \quad (9)$$

and the Fourier coefficients corresponding to the p-polarized waves, $A_p^{(n)}(q_{\parallel})$, are rescaled so as to separate their singular behavior at the plasmon wave vector $q_{\parallel} = k_{\parallel}$ [the function $f_p(q_{\parallel})$ has a simple zero at $q_{\parallel} = k_{\parallel}$ and $f_p(k_{\parallel}) = 0$],

$$A_p^{(n)}(q_{\parallel}) = \frac{a_p^{(n)}(q_{\parallel})}{f_p(q_{\parallel})}. \quad (10)$$

Note that since the scattering amplitudes $A_p^{(n)}(\mathbf{q}_{\parallel})$ have a simple pole at $q_{\parallel} = k_{\parallel}$, the reduced scattering amplitudes $a_p^{(n)}(q_{\parallel})$ are bounded functions. Finally, by substituting Eqs. (9) and (10) into relation (4) one obtains the following set of coupled integral equations:

$$a_p^{(n)}(p_{\parallel}) + \frac{1}{2\pi}\int_0^{\infty} dq_{\parallel}q_{\parallel}\left[\frac{h_{pp}^{(n)}(p_{\parallel},q_{\parallel})}{f_p(q_{\parallel})}a_p^{(n)}(q_{\parallel}) + h_{ps}^{(n)}(p_{\parallel},q_{\parallel})A_s^{(n)}(q_{\parallel})\right] = -h_{pp}^{(n)}(p_{\parallel},k_{\parallel}), \quad (11a)$$

$$f_s(p_\parallel)A_s^{(n)}(p_\parallel) + \frac{1}{2\pi}\int_0^\infty dq_\parallel q_\parallel \left[\frac{h_{sp}^{(n)}(p_\parallel,q_\parallel)}{f_p(q_\parallel)} a_p^{(n)}(q_\parallel) + h_{ss}^{(n)}(p_\parallel,q_\parallel)A_s^{(n)}(q_\parallel) \right] = -h_{sp}^{(n)}(p_\parallel,k_\parallel), \tag{11b}$$

where

$$h_{ss}^{(n)}(p_\parallel,q_\parallel) = \frac{1}{2}\frac{\omega^2}{c^2}(N_{n-1}+N_{n+1}), \tag{12a}$$

$$h_{pp}^{(n)}(p_\parallel,q_\parallel) = N_n p_\parallel q_\parallel - \frac{1}{2}\alpha(p_\parallel)\alpha_0(q_\parallel)(N_{n-1}+N_{n+1}), \tag{12b}$$

$$h_{sp}^{(n)}(p_\parallel,q_\parallel) = -\frac{1}{2}\frac{\omega}{c}\alpha_0(q_\parallel)(N_{n-1}-N_{n+1}), \tag{12c}$$

$$h_{ps}^{(n)}(p_\parallel,q_\parallel) = \frac{1}{2}\frac{\omega}{c}\alpha_0(q_\parallel)(N_{n-1}-N_{n+1}), \tag{12d}$$

and

$$N_m = \frac{2\pi}{\alpha(p_\parallel)-\alpha_0(q_\parallel)}\int_0^\infty \{e^{[\alpha(p_\parallel)-\alpha_0(q_\parallel)]\zeta(x_\parallel)}-1\} \times J_m(p_\parallel x_\parallel)J_m(q_\parallel x_\parallel)x_\parallel dx_\parallel. \tag{13}$$

Equations (11) are solved numerically for the scattering amplitude coefficients $a_p^{(n)}(p_\parallel)$ and $A_s^{(n)}(p_\parallel)$ and, subsequently, by using the Fourier expansions in Eq. (9), the scattering amplitudes $A_{s,p}(\mathbf{p}_\parallel)$ are determined. These scattering amplitudes fully determine the distribution of the electric field in the spatial region $x_3 \geq \zeta(\mathbf{x}_\parallel)$, at the FF, as shown by Eq. (1).

B. Light scattering at the second harmonic

The complete description of the spatial distribution of the electromagnetic field at the FF allows one to determine the field distribution at the SH. Thus, according to the phenomenological model that is used to describe the physical properties of the SHG at the interface between two centrosymmetric media, the generated SH has two sources, namely, a surface nonlinear polarization localized within a thin surface layer at the interface between the two media and a nonlocal polarization originating from bulk magnetic dipoles and electric quadrupoles. Although the two media are centrosymmetric and thus electric-dipole transitions are not allowed, the inversion symmetry is broken in the thin layer at the interface between the two media and therefore a sheet of nonlinear surface polarization at the SH, $\mathbf{P}_s^{(2\omega)}(\mathbf{r})$, is induced at this interface. This nonlinear polarization is related to the electric field at the FF by a second-order nonlinear susceptibility tensor,

$$\mathbf{P}_s^{(2\omega)}(\mathbf{r}) = \hat{\chi}_s^{(2)}:\mathbf{E}^{(\omega)}(\mathbf{r})\mathbf{E}^{(\omega)}(\mathbf{r})\,\delta[x_3-\zeta(\mathbf{x}_\parallel)], \tag{14}$$

where $\hat{\chi}_s^{(2)}$ is the surface second-order susceptibility and the Dirac function describes the surface characteristic of the source polarization.

In the case of homogeneous isotropic media excited by plane waves the bulk nonlocal nonlinear polarization can be expressed as[47,48] $\mathbf{P}_{\text{bulk}}^{(2\omega)}(\mathbf{r}) = \gamma\nabla[\mathbf{E}^{(\omega)}(\mathbf{r})\cdot\mathbf{E}^{(\omega)}(\mathbf{r})]$, where $\gamma = e[1-\epsilon(\omega)]/32\pi m\omega^2$ and e and m are the charge and mass of the electron, respectively. As has been demonstrated,[49] the longitudinal nature of this nonlinear polarization makes it that its contribution to the SHG is indistinguishable from that of the surface nonlinear polarization given in Eq. (14). In practice, this contribution is accounted for by rescaling the components of the surface susceptibility $\hat{\chi}_s^{(2)}$ so as to include the contributions of both the surface and bulk polarizations. Nevertheless, in the case of metals these two nonlinear polarization sources have largely different relative contributions to the SHG process, especially if ω is close to the frequency of resonantly excited SPPs. Thus at this frequency, the contribution of the surface nonlinear polarization to the SHG is enhanced significantly more than that of the bulk source,[50] and therefore the bulk contribution can be neglected. Indeed, recent experiments have demonstrated that in the case of metals with good, i.e., low-loss optical properties (Ag and Au) the surface nonlinear susceptibility is about 2 orders of magnitude larger than the bulk one.[51]

In most cases of practical interest, the metal/vacuum interfaces possess an isotropic mirror-symmetry plane perpendicular to the interface. Under these circumstances, the surface nonlinear susceptibility $\hat{\chi}_s^{(2)}$ has only three independent components, which are $\hat{\chi}_{s,\perp\perp\perp}^{(2)}$, $\hat{\chi}_{s,\perp\parallel\parallel}^{(2)}$, and $\hat{\chi}_{s,\parallel\parallel\perp}^{(2)} = \hat{\chi}_{s,\parallel\perp\parallel}^{(2)}$, where $\perp$ and $\parallel$ refer to normal and perpendicular directions to the surface, respectively. In our calculations, we assume the following values for the independent components of the susceptibility tensor $\hat{\chi}_s^{(2)}$, $\hat{\chi}_{s,\perp\perp\perp}^{(2)} = 5.02\times10^{-18}$ m^2/V, $\hat{\chi}_{s,\perp\parallel\parallel}^{(2)} = -2.54\times10^{-21}$ m^2/V, and $\hat{\chi}_{s,\parallel\parallel\perp}^{(2)} = \hat{\chi}_{s,\parallel\perp\parallel}^{(2)} = 1.13\times10^{-20}$ m^2/V.[51] However, it should be noted that in certain cases the metal/vacuum interface lacks a mirror-symmetry plane, namely, when chiral molecules are adsorbed at the interface or in the case of nanopatterned metallic surfaces.

Since the source of the electromagnetic field at the SH is the surface nonlinear polarization $\mathbf{P}_s^{(2\omega)}(\mathbf{r})$, we can fully characterize the SHG process once we know the multipole moments associated with the charge distribution generated by this nonlinear polarization. As the characteristic size a of the nanodefect is considerably smaller than the plasmon wavelength, $k_\parallel(\omega)a \ll 1$, we have restricted our calculations to multipoles up to the second order, that is, the electric dipole moment, the magnetic dipole moment, and the electric quadrupole moment; they are defined by the following relations:[52]

$$\mathbf{p} = \int \mathbf{P}^{(2\omega)}(\mathbf{r}')d^3\mathbf{r}', \tag{15a}$$

$$\mathbf{m} = -\frac{i\omega}{2}\int \mathbf{r}'\times\mathbf{P}^{(2\omega)}(\mathbf{r}')d^3\mathbf{r}', \tag{15b}$$

$$\mathbf{Q}(\mathbf{n}) = \int \{3\{(\hat{\mathbf{r}}\cdot\mathbf{r}')\mathbf{P}^{(2\omega)}(\mathbf{r}') + [\hat{\mathbf{r}}\cdot\mathbf{P}^{(2\omega)}(\mathbf{r}')\mathbf{r}']\} - 2[\mathbf{r}'\cdot\mathbf{P}^{(2\omega)}(\mathbf{r}')]\hat{\mathbf{r}}\}d^3\mathbf{r}'. \tag{15c}$$

Since we are only interested in the SH generated by the

nanodefect, the integration region in Eqs. (15) for a Gaussian defect is chosen to be $L=3.5R$, as illustrated in Fig. 1. For the case of spherical cap and cylinder, the domains of integration are chosen to be $\zeta(\mathbf{x}_\parallel)\neq 0$, that is, $L=2\varrho$ for the spherical cap and $L=2R$ for the cylinder. It should be noted that in our study we do not consider the SHG from the entire flat surface, which has been extensively studied, because it contributes only a uniform background illumination.[3]

The angular distribution for the radiated power at the SH, originating from the multipoles described by Eqs. (15), is given by the following equations:[53]

$$\frac{dP_{\mathrm{ed}}}{d\Omega}=\frac{Z_0c^2K^4}{32\pi}|(\mathbf{n}\times\mathbf{p})\times\mathbf{n}|^2, \tag{16a}$$

$$\frac{dP_{\mathrm{md}}}{d\Omega}=\frac{Z_0K^4}{32\pi}|(\mathbf{n}\times\mathbf{m})\times\mathbf{n}|^2, \tag{16b}$$

$$\frac{dP_{\mathrm{eq}}}{d\Omega}=\frac{Z_0c^2K^6}{1152\pi^2}|[\mathbf{n}\times\mathbf{Q}(\mathbf{n})]\times\mathbf{n}|^2, \tag{16c}$$

where P_{ed}, P_{md}, and P_{eq} correspond to the power radiated by the electric dipole, magnetic dipole, and electric quadrupole, respectively. $K=2\omega/c$ is the wave vector at the second harmonic and $Z_0=\sqrt{\mu_0/\epsilon_0}$ is the vacuum impedance. As is well known from classical electrodynamics, at longer wavelengths the main contribution to the emitted energy comes from the electric-dipole moment ($P_{\mathrm{ed}}\sim\lambda^{-4}$), whereas at smaller wavelengths the radiated energy comes primarily from the magnetic and quadrupole moments ($P_{\mathrm{md}},P_{\mathrm{qd}}\sim\lambda^{-6}$). Finally, calculating these multipoles allow us to determine not only the radiative field at the SH but also the near field; the corresponding near-field formulas are not presented here as their expressions are rather long and cumbersome.

C. Numerical approach

To solve Eqs. (11) numerically, we follow a procedure described in Ref. 2. Thus, this system of coupled equations is discretized on a uniform computational grid that spans the domain $q_\parallel,p_\parallel\in(0,\Lambda_{\max})$, the step size of the computational grid being $\Delta q_\parallel$. To reach convergence of the numerical results, ~1500 grid points are necessary, whereas the upper limit of the wave vectors $p_\parallel$ and $q_\parallel$, $\Lambda_{\max}$, is chosen to be in the range of $20/R-70/R$. In addition, the computational grid is constructed in such a way that the point $k_\parallel$ is one of the grid points.

In the discretization process, the integrals in Eqs. (11) are calculated as a sum of integrals defined over the intervals between adjacent grid points, each of these integrals being then approximated as the product between the integrand evaluated at the midpoint of the interval and the size of the interval, $\Delta q_\parallel$. As previously explained, the integral Eqs. (11) have a singularity (a simple pole) at $q_\parallel=k_\parallel$. This singular point is treated separately, the corresponding integral being calculated analytically. As a result of this discretization procedure, Eqs. (11) are cast into two linear coupled matrix equations, which are solved by using standard numerical techniques. The corresponding disctretized equations can be written in the following form:

$$a_p^{(n)}(p_i)+\frac{1}{2\pi}\sum_j\Delta qq_j\left[\frac{h_{pp}^{(n)}(p_i,q_j)}{f_p(q_j)}a_p^{(n)}(q_j)+h_{ps}^{(n)}(p_i,q_j)A_s^{(n)}\times(q_j)\right]=-h_{pp}^{(n)}(p_i,k_\parallel), \tag{17a}$$

$$f_s(p_i)A_s^{(n)}(p_i)+\frac{1}{2\pi}\sum_j\Delta qq_j\left[\frac{h_{sp}^{(n)}(p_i,q_j)}{f_p(q_j)}a_p^{(n)}(q_j)+h_{ss}^{(n)}\times(p_i,q_j)A_s^{(n)}(q_j)\right]=-h_{sp}^{(n)}(p_i,k_\parallel), \tag{17b}$$

where i and j indices are the grid points. Furthermore, in the case of a Gaussian-shaped defect, the integrals N_m defined by Eq. (13) can be expressed as a series of Bessel functions of the second kind, I_m,

$$N_m(p_\parallel,q_\parallel)=\pi AR^2\sum_{n=1}^{\infty}\frac{\{[\alpha(p_\parallel)-\alpha_0(q_\parallel)]A\}^{n-1}}{n\cdot n!}\times e^{-(p_\parallel^2+q_\parallel^2)R^2/4n}I_m\left(\frac{p_\parallel q_\parallel R^2}{2n}\right). \tag{18}$$

For the hemisphere- and cylinder-shaped defects the integral that defines the functions $N_m(p_\parallel,q_\parallel)$ are calculated numerically by using an adaptive integration algorithm.[54] Moreover, in the case of cylindrical nanodefects, in order to resolve the strongly inhomogeneous electromagnetic field near the sharp corners, a considerably large number of grid point must be used, with the result of a slow convergence rate of the numerical algorithm. In order to overcome this problem, a numerical procedure was employed that in effect smoothes out the top edge of the cylinder, namely, the shape function $\zeta(\mathbf{x}_\parallel)$ was multiplied by the function shape factor $1-\frac{1}{\cosh[p_1(p_2R-x_\parallel)]}$, with $p_1=0.6\times10^8$ and $p_2=1.12$.

Finally, once the complete distribution of the electromagnetic field at the FF is determined through the method just described, the scattering process at the SH is numerically characterized as follows. First the surface nonlinear polarization $\mathbf{P}_s^{(2\omega)}(\mathbf{r})$ is calculated using Eq. (14), and subsequently the multipoles are determined from Eqs. (15). The spatial distribution of the electromagnetic field at the SH and the corresponding emitted power are then calculated by using Eqs. (16).

III. RESULTS AND DISCUSSION

In this section we present and discuss the main results pertaining to the spatial distribution of near and far field, as well as the spatial pattern of the scattered light, both at the FF and the SH.

A. Field distribution and scattered light: Fundamental frequency

The theoretical formalism presented in Sec. II A provides a full description of the distribution of the electromagnetic

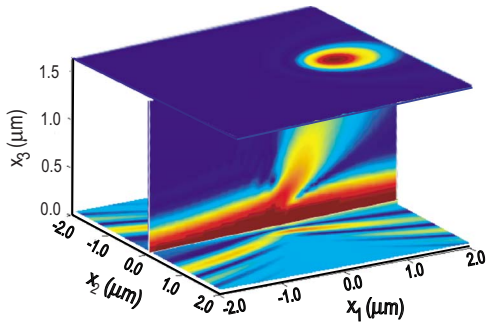

FIG. 2. (Color online) Electric field distribution corresponding to the scattering of a SPP off a Gaussian nanodefect with $R=200$ nm and $h=-50$ nm where only the scattered light is shown. The wavelength of the incident SPP is $\lambda=328$ nm.

field, both in the close proximity of the defect (the near field), as well as far from the scatterer (the far field). A generic example of the spatial distribution of the field amplitude at the FF, $|\mathbf{E}^{\uparrow}(\mathbf{r};\omega)|$, corresponding to a Gaussian indentation, is presented in Fig. 2. Among other things, this figure clearly shows the transition between the near field, seen as a series of ripples that are formed through the interference between the incident plasmon field and the scattered field and the far field, which is seen as an emerging beam of scattered light (a nanoflashlight) emitted by the defect. The angle of this flashlight "beam" with respect to the surface normal is a result of momentum matching between the SPP and scattered light momenta and a characteristic reciprocal vector of the scatterer, i.e., π/R, much as is the case of plasmon scattering from a surface diffraction grating.[1] Note that the width of the emitted beam, measured in a transverse plane located at 1.5 μm above the metallic surface, is only a few hundreds nanometers. Hence the plasmon scattering by metallic nanodefects could provide an interesting and flexible approach to generate and manipulate subwavelength optical beams, an idea discussed in Ref. 2.

As an interesting aside, the property that the shape of the defects considered here is invariant to rotation transformations implies that the scattering coefficients $A_{p,s}^{(n)}(q_{\parallel})$ defined by Eq. (9) obey the symmetry relation $|A_{p,s}^{(n)}(q_{\parallel})|=|A_{p,s}^{(-n)}(q_{\parallel})|$, and therefore the total angular momentum of the scattered electromagnetic field is zero. However, it can be easily seen that in the case of chiral scatterers the just mention symmetry relation no longer holds, and thus the scattered field, in particular the nanoflashlight seen in Fig. 2, will have a finite angular momentum. One immediate consequence of this effect is that the scattering of SPPs from chiral defects can be readily used to generate subwavelength optical beams carrying angular momentum, namely, optical nanotweezers.

Deeper insight into the characteristics of the plasmon scattering at the FF is provided by the frequency dependence of the total scattering cross sections of SPPs and light. Since the total energy is conserved in the scattering process, as the imaginary part of the dielectric constant has been set to zero, the total scattering cross sections of SPPs and light can be used to calculate the amount of energy absorbed from the incident SPP wave. This could be important in the case of multiple scatterers that are located not very close to each

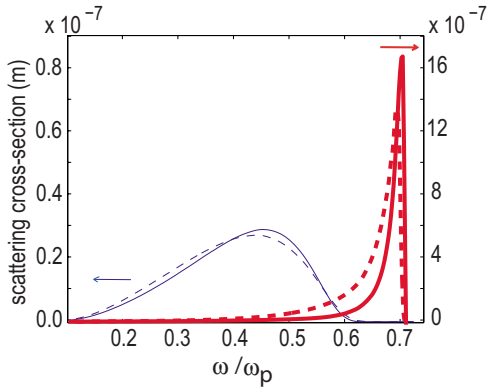

FIG. 3. (Color online) Total scattering cross section of light and SPP for both indentation ($h<0$, solid line) and protuberance ($h>0$, dash line). The defect parameters are $|h|=50$ nm and $R=200$ nm. The red (thick) and blue (thin) curves correspond to the scattering cross section of SPPs and light, respectively.

other, such that multiple-scattering processes can be neglected since it would allow one to calculate the corresponding absorption coefficient of the incident SPP wave. Thus, using relations (A5) in the Appendix, we have calculated the spectra of these scattering cross sections, both for indentations and protuberances. Note that the scattering cross section corresponding to the emitted radiation contains the contribution of both the *s*- and *p*-polarized waves. The results of these calculations, summarized in Fig. 3, lead us to several important conclusions. But before discussing the results note that the general shape and appearance of these two scattering cross sections is similar to that presented earlier by the Maradudin and co-workers,[2,43] although the greater computation resources available at present allows a fuller spectral range to be examined. First, both spectra show a resonant behavior, in both cases the scattering process being most efficient at a certain resonant frequency. The two resonant frequencies are very different from each other, and thus one can infer that the two scattering processes are only weakly coupled.[55] More specifically, whereas the generation of radiative modes can be viewed as the result of the creation of spatial inhomogeneities in the incoming field, at the location of the defect, the scattered surface plasmons are generated via the excitation of localized plasmon modes supported by the surface defect. This dichotomy in the scattering process also explains the markedly different width of the SPP and light spectra of the corresponding cross sections. In addition, a comparison of the peak scattering cross sections suggests that the scattering of the incident SPP into SPP waves is a much more efficient process as compared to the scattering of the incident SPP into radiation, the corresponding ratio of the cross sections being ~ 5. This result is explained by the fact that, due to their similar characteristics, the overlap between the electromagnetic field of the incident and scattered SPP waves is larger than the overlap between the fields of the incident SPP wave and the emitted radiation.

Figure 3 also shows that surface indentations are more effective in scattering the incident SPP, as compared with protuberances, a result that can be attributed to the cavity effect associated with such surface defects. Moreover, the

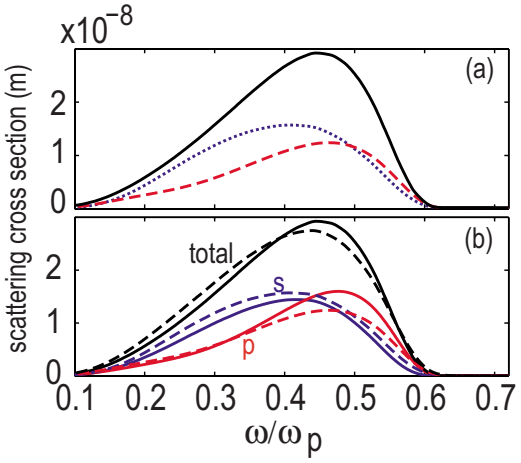

FIG. 4. (Color online) Dependence of the scattering cross section of light on the size of the Gaussian defect and polarization of the scattered light. The curves in the panel (a) correspond to $R=200$ nm and $h=-50$ nm (solid curve), $R=200$ nm and $h=-20$ nm (dash curve), $R=150$ nm and $h=-20$ nm (dotted curve). Panel (b) shows the spectra of the scattering cross sections corresponding to $R=200$ nm and $|h|=50$ nm: the solid (dash) curves correspond to $h<0$ ($h>0$). As indicated, the black curves correspond to the total scattering cross section, whereas the blue and red curves correspond to the s- and p-polarized light, respectively.

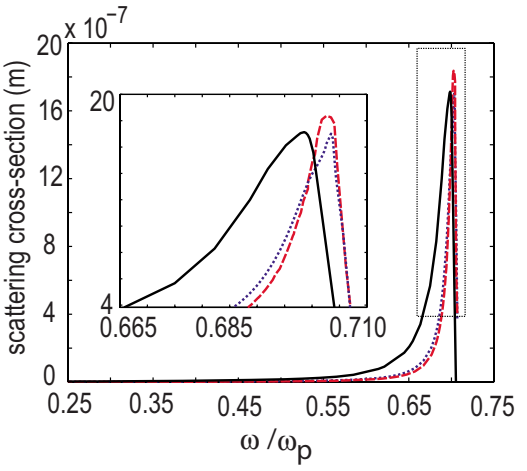

FIG. 5. (Color online) Dependence of the scattering cross section of SPPs on the size of the Gaussian defect. The curves correspond to $R=200$ nm and $h=-50$ nm (solid curve), $R=200$ nm and $h=-20$ nm (dash curve), $R=150$ nm and $h=-20$ nm (dotted curve).

spectra of the scattering cross sections of both SPPs and light show a steep decrease near $\omega/\omega_p \sim 0.7$, which is due to the fact that surface SPP waves at the metal/vacuum interface cannot exist if $\omega > \frac{\omega_p}{\sqrt{2}}$.

We have also investigated the dependence of the scattering cross sections on the size of the surface defect. The results corresponding to the scattering cross section of light are summarized in Fig. 4(a). Thus one can observe that in the case of shallow surface defects the amount of radiated light decreases as the radius of the defect increases, which suggests that in the case of larger defects the field can easier readjust to the shape of the defect and thus it is perturbed to a smaller extent. However, if one compares the amount of light scattered by defects with the same radius R but different depth h one observe that more light is emitted by defects with larger depth. Again, this result is explained by the fact that the larger the depth of a surface defect, the stronger the perturbation of the incident plasmon field; although not shown, this same behavior follows when varying the height of protuberance.

As we have discussed, unlike the 1D case, in the case of 2D surface defects the emitted light cannot only be p polarized but also s polarized. The spectra of the total scattering cross section as well as the corresponding spectra of the s- and p-polarized light are shown in Fig. 4(b). Thus, it can be seen from this figure that the spectra corresponding to the two polarizations show a similar resonant behavior; however, the two resonant frequencies have slightly different values. In addition, our calculations show that at low frequency (long-wavelength side of the spectra) the radiated light is predominantly s polarized, whereas the light emitted at high frequencies (at the blue side of the spectrum) is predominantly p polarized.

Similar studies have been done of the dependence of the peak SPP scattering cross section and the width of its spectrum on the width and depth or height of the defect. The main results, plotted in Fig. 5, support the general conclusion according to which the incident SPP wave generates SPP modes localized at the site of the defect, which subsequently decay into outgoing SPP waves. Thus, Fig. 5 shows that the width of the spectrum of the scattering cross section decreases with the depth of the defect. As expected, deeper defects are more effective in capturing and thus re-emitting the incident SPP wave, an effect that leads to the broadening of the SPP scattering cross-section spectra with the width of the defect. On the other hand, the scattering cross section depends only slightly on the radius of the defect.

A better understanding of scattering of the incident SPP, at the FF, can be achieved by analyzing the distribution of the electromagnetic field in the proximity of the surface defect. In this connection, Fig. 6 shows the field distribution in two horizontal sections, one at a distance that is only a fraction of the wavelength of the plasmon and the other one located a few wavelengths away from the metallic surface. Note that the plots in Fig. 6 do not contain the field of the incident SPP wave. This figure clearly illustrates the transition from the near field to far field as well as the strong dependence of the electromagnetic field on the polarization of the emitted field. Thus, as expected, in the case of the s-polarized light, the field is predominantly located at the position of the surface defect. This behavior is a direct consequence of the fact that the SPP waves are p polarized, and thus the s-polarized field cannot propagate along the vacuum/metal interface. Moreover, Fig. 6 shows that in the case of the s-polarized scattered light the electric field vanishes in the plane $x_2=0$. To understand this property, note that the electric field of the s-polarized scattered light at the plane $x_2=0$ is perpendicular on this plane, and thus the symmetry considerations require that it vanishes within this plane. In addition the electric field for p-polarized light has a large value even a few wavelengths away from the surface defect. This electric field is

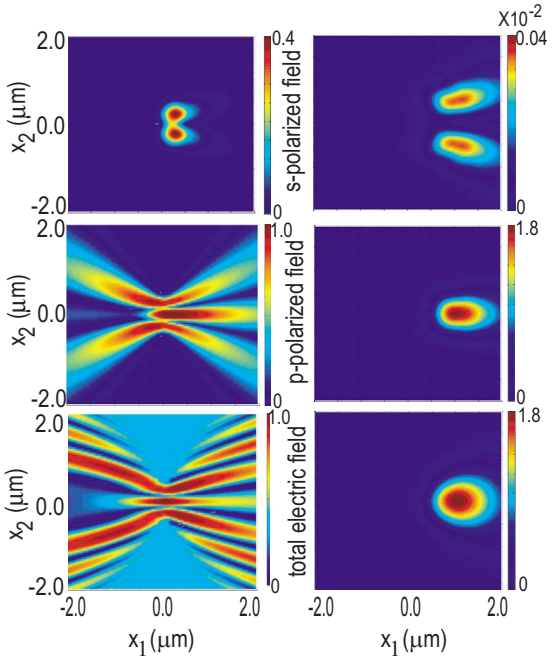

FIG. 6. (Color online) Near- to far-field transition corresponding to a Gaussian surface defect with $R=200$ nm and $h=-50$ nm. The incident SPP wavelength is $\lambda=328$ nm. The panels on the left and on the right correspond to horizontal plane sections at $x_3=0.2$ μm and $x_3=1.2$ μm, respectively.

radiated by the outgoing surface SPP waves that are generated in the scattering process. Also, note that the spatial distribution of the total field is similar to that of the p-polarized light, which suggests that, at this wavelength, the radiated light in the nanobeam directed in the $x_2=0$ plane is predominantly p polarized. S-polarized light is emitted at two angles with respect to this plane and is thus more diffuse in the $x_3=1.2$ μm plane shown here.

We have also investigated the dependence of the SPP-surface defect scattering process on the specific shape of the defect. In particular, we have considered the Gaussian, cylindrical, and hemispherical defects. The main results of this analysis are presented in Fig. 7, which shows the frequency dependence of the scattered light corresponding to these three shapes of the surface defect. As expected, the scattering cross section of light emitted by the Gaussian and hemispherical defects have similar spectral characteristics, namely, a broad spectrum with a maximum at a certain resonant frequency. Unlike the case of these two types of surface defects, the spectra corresponding to cylindrical defects, i.e., cylindrical holes or pillars, present a series of sharp well-defined maxima which become more closely spaced as the frequency approaches the asymptotic limit $\omega=\frac{\omega_p}{\sqrt{2}}$. These spectral peaks can be associated with the excitation of plasmon modes with a vanishing longitudinal (along the x_3 axis of the cylinder) propagation constant at the surface of the cylindrical defects. Indeed, the propagation constant of the incident surface plasmon lies in the surface plane, and therefore any modes excited in the x_3 plane for a cylindrical defect must have a vanishing longitudinal propagation constant. As it is well known,[56,57] these modes form a sharp

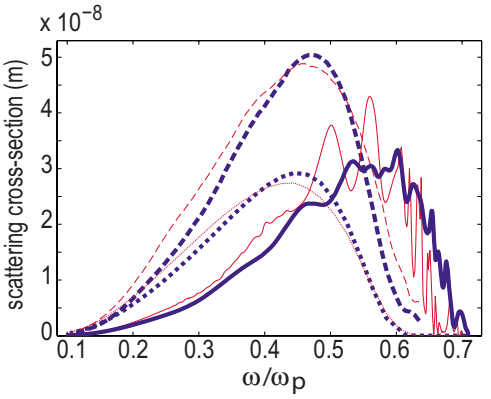

FIG. 7. (Color online) Scattering cross sections corresponding to cylindrical ($R=200$ nm and $|h|=20$ nm, solid curves), hemispherical ($R=600$ nm and $|h|=50$ nm, dash curves), and Gaussian ($R=200$ nm and $|h|=20$ nm, dotted curves) surface defects. The thick and thin curves correspond to $h<0$ and $h>0$, respectively.

discrete spectrum with the mode frequency asymptotically approaching the limit frequency of $\frac{\omega_p}{\sqrt{2}}$, irrespective of the radius of the cylinder.

Our calculations show not only that the spectra of the scattering cross sections depend on the particular shape of the defect but also that the field distribution is strongly dependent on the geometry of the defect. This property, which can have a series of applications to near-field optical microscopy, is illustrated by the results summarized in Fig. 8. This figure clearly shows that both the near field and the far-field generated in the scattering process, at the FF, are strongly dependent on the shape of the defect. For example, it can be seen that, unlike the case of a Gaussian or hemispherical defect, two nanobeams are emitted in the case of a cylindrical defect.

B. Field distribution and scattered light: Second harmonic

The theoretical formalism presented in Sec. II B allows one to determine the spatial distribution of the electric field

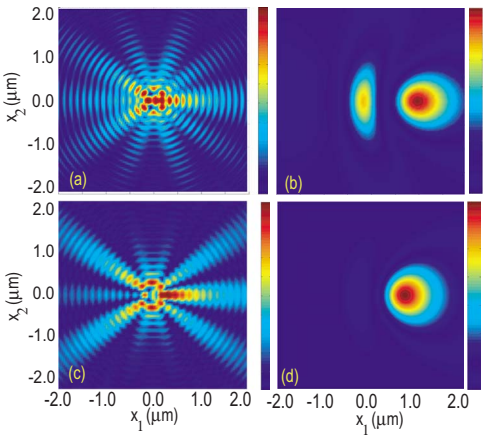

FIG. 8. (Color online) Near-field and far-field distributions corresponding to cylindrical ($R=200$ nm and $h=-20$ nm, top panels) and hemispherical ($R=600$ nm and $h=-50$ nm, bottom panels) surface defects. The panels on the left and on the right correspond to horizontal plane sections at $x_3=0.2$ μm and $x_3=1.2$ μm, respectively. The incident SPP wavelength is $\lambda=328$ nm.

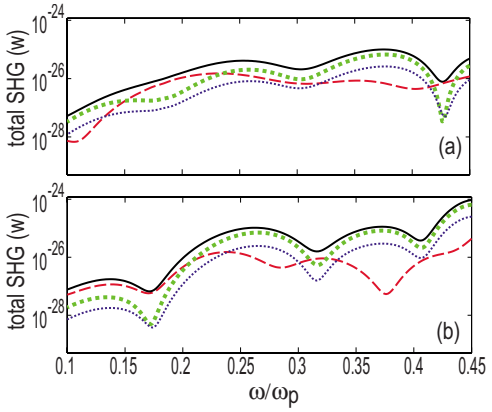

FIG. 9. (Color online) Spectra of the SH radiated upon the scattering of SPP waves off Gaussian surface defects. Panels (a) and (b) correspond to indentations ($h=-50$ nm) and protuberances ($h=50$ nm), respectively. In both panels, $R=200$ nm and the spectra in both panels correspond to the electric dipole moment (thin dash curves), the magnetic dipole moment (thick dotted curves), the electric quadrupole moment (thin dotted curves), and the total SHG (thin solid curves).

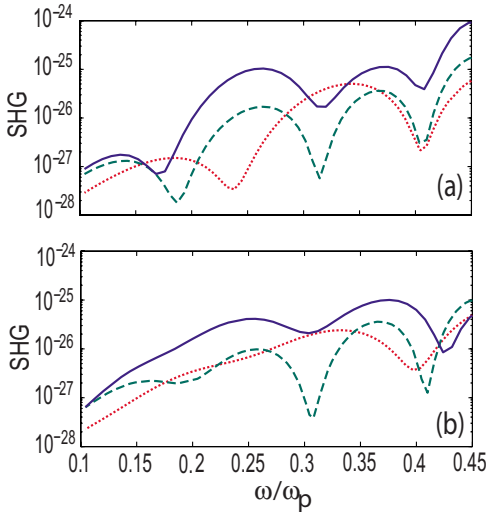

FIG. 10. (Color online) Dependence of the total SHG on the size of Gaussian surface defects. Panels (a) and (b) correspond to protuberances ($h>0$) and indentations ($h<0$), respectively. In both panels, the parameters of the defect are: $R=200$ nm and $|h|=50$ nm (solid curves), $R=200$ nm and $|h|=20$ nm (dash curves), and $R=150$ nm and $|h|=20$ nm (dotted curves).

at the SH and the corresponding scattering cross section, once the electric field at the FF has been calculated. In addition, our theoretical model allows us to study the relative contribution of the multipole moments to the total amount of light generated at the SH.

A generic example that illustrates how our theoretical model can be applied to study the generation of SH via the scattering of SPP waves by surface defects is presented in Fig. 9. Thus, this figure shows the spectra of the radiated SH, the surface defects considered being Gaussian-shaped indentations and protuberances. Our theoretical formalism allows us to separate the contribution of each multipole moment to the total generated SHG so that we show in Fig. 9 the spectrum of each of all these moments (up to the second order). Recall, however, that our approach is only valid if the wavelength is larger than the characteristic size of the defect when the multipole series expansion converges; we have used this criterion in choosing the frequency range in which we have calculated the scattering cross section at the SH. As expected, our calculations show that the SH generated at short wavelengths is predominantly due to the higher-order multipole moments (magnetic dipole and electric quadrupole), whereas at long wavelengths (low frequency) the SH is primarily generated by the induced electric dipoles. In addition, it can be seen that the frequencies of the maxima and minima in the spectra corresponding to the magnetic dipole and electric quadrupole are the same; in fact overall, these spectra exhibit nearly identical spectral variation. However, the spectrum corresponding to the electric dipole shows a quite different frequency dependence, a fact that is explained by the particular dependence on wavelength of the power radiated by the induced multipole moments [see Eq. (16)]. Note also that the total amount of generated SH increases with the frequency of the incident SPP wave. Indeed, as the frequency increases the incident SPP wave has a shorter wavelength and thus interacts more strongly with the surface defect. Consequently, the induced multipole moments have a larger magnitude. Importantly, the spectral characteristics of the radiated power at the FF are significantly different from those corresponding to the SH, which further illustrates the differences in the physical phenomena involved in the radiation process at the two frequencies.

We have also investigated the dependence of the spectra of the generated SH on the geometrical parameters of the surface defect. The results corresponding to a Gaussian surface defect are summarized in Fig. 10. This figure shows that larger defects lead to the generation of a larger SH signal. This result is an expected dependence of the SHG on the size of the defect since in the case of larger defects the nonlinear surface polarization is induced over a larger area, and therefore the multipole moments that generate light at the SH are larger. Also, Fig. 10 suggests that the frequencies at which the SH spectra have minima are primarily determined by the radius of the defect, the height (depth) h having only a marginal influence on the location of these frequencies.

Our calculations show that, unlike the case of the FF, the spectra of the radiated light at the SH depend to a lesser extent on the shape of the surface defect. This conclusion is illustrated by Fig. 11, which shows the spectra corresponding to cylindrical and hemispherical defects, for both $h>0$ and $h<0$. The general characteristics of these spectra are very similar to those corresponding to the Gaussian surface defects, part of the observed differences being attributable to the fact that the defects have different size. Indeed, the amount of radiation emitted at the SH depends primarily on the magnitude of the induced multipole moments, and thus one expects that the general characteristics of the corresponding spectra would depend only slightly on the shape of the surface defect.

One of the important applications of the theoretical formalism presented here is that the spectral characteristics of the radiation emitted at the SH can be used to extract infor-

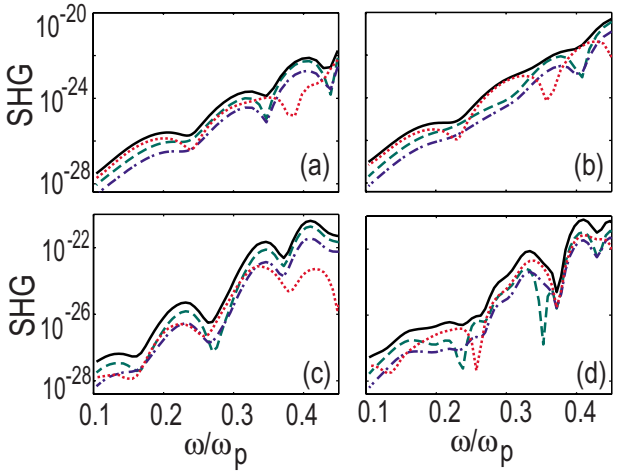

FIG. 11. (Color online) Top and bottom panels show the SHG corresponding to cylindrical and hemispherical surface defects, respectively. In all panels, the spectra correspond to the electric dipole moment (dotted curves), the magnetic dipole moment (dash curves), the electric quadrupole moment (dotted-dash curves), and the total amount of generated SH (solid curves).

mation about the geometry of the surface defects and their surface properties. For example, since the angular distribution of the radiation emitted by electric dipoles, electric quadrupoles, and magnetic dipoles are quite different from each other, the angular distribution of the total radiated light at the SH will depend strongly on the relative strength of the magnitude of these induced multipoles. Therefore, the angular distribution of the total light emitted at the SH can provide valuable information about the shape and surface properties of the defect. This idea is illustrated in Fig. 12, where we show the angular distribution of the light emitted at the SH, as well as the angular distribution corresponding to the electric dipole, electric quadrupole, and magnetic dipole. Note that in this figure the parameters of the surface defect and the wavelength of the incident SPP wave have been chosen such that the amount of light radiated by each of the three multipoles has a comparable magnitude, and therefore the angular distribution of the total radiated light is different from each

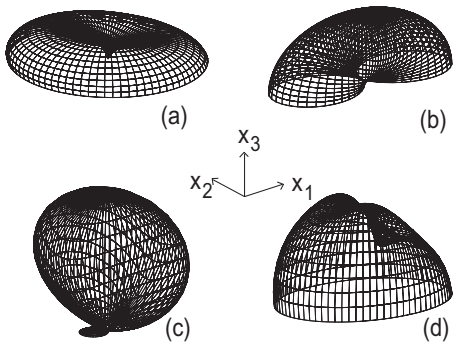

FIG. 12. Angular distribution of the power emitted at the SH. The panels correspond to a Gaussian surface defect with $R=200$ nm and $h=-50$ nm, and an incident SPP wave with wavelength $\lambda=1012$ nm. The panels correspond to (a) the electric dipole momentum, (b) the magnetic dipole momentum, (c) the electric quadrupole moment, and (d) the total SH.

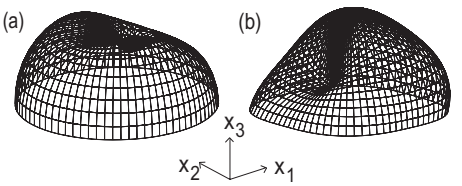

FIG. 13. Angular distribution of the power emitted at the SH. The panels correspond to a cylindrical (left) and hemispherical (right) surface defects, the wavelength of the incident SPP being $\lambda=1012$ nm. The defect parameters are (a) $R=200$ nm and $h=-20$ nm, and (b) $R=600$ nm and $h=-50$ nm.

of the angular distributions corresponding to the three multipoles. However, in the case in which one of the multipoles dominates, the total angular distribution of the SH will be similar to the angular distribution of that multipole and thus this information can be used to determine the properties of the surface defect.

The angular distribution of the power emitted at the SH can be used not only to infer which is the dominant multipole that generates light at the SH but also to obtain information about the shape of the surface defect. As illustrated in Fig. 13, this is possible because the angular distribution of the power radiated at the SH is strongly dependent on the shape of the surface defect. Thus, as Fig. 13 shows, the angular distribution of the power emitted by a cylindrical defect is very different from the angular dependence of the power emitted by an hemispherical defect. Consequently, measuring the angular distribution of the power generated at the SH could represent a powerful surface probing tool.

In addition to the angular dependence of the power emitted at the SH, the spatial distribution of the near field at the SH can provide valuable information about the properties of the surface defect. In particular, the spatial distribution of the near field at the SH depends on the shape of the surface defect and the nature of the surface (through the surface susceptibility), and thus near-field surface optical microscopy measurements at the SH can be used as an effective tool to study the properties of surface defects.[39] As an example, we show in Fig. 14 the spatial distribution of the near field at the SH, corresponding to a Gaussian defect. Our calculations show clearly that such field distributions are strongly depen-

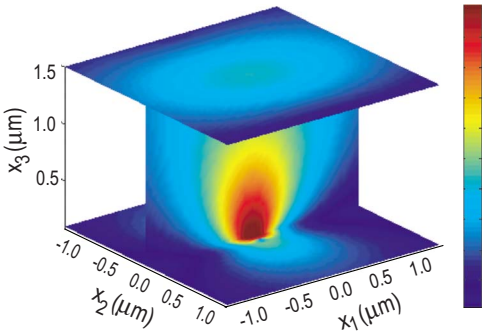

FIG. 14. (Color online) Electric field distribution corresponding to the scattering of a SPP off a Gaussian surface defect with $R=200$ nm and $h=-50$ nm. The wavelength of the incident SPP is $\lambda=328$ nm.

dent on the shape of the surface defect and the wavelength of the incident SPP wave, a property explained by the fact that the relative strength of the induced multipoles that determine this field distribution is strongly dependent on these parameters. Arguments similar to those just presented in connection to the angular distribution of the power radiated at the SH allow us to conclude that the near field at the SH can be used to retrieve additional information, which is not contained in the field distribution at the FF.

IV. CONCLUSIONS

In conclusion, we have presented a comprehensive analysis of the physical characteristics of the SH generated as a result of the scattering of SPP waves off surface metallic nanodefects with radial symmetry. Our analysis, based on a set of coupled-reduced Rayleigh equations, can be applied to surface nanodefects of arbitrary shape; in particular, we have investigated surface nanodefects with three different geometries that are important in practical applications, namely, Gaussian, hemispherical, and cylindrical nanodefects. It should be noted, however, that the Rayleigh scattering formalism presented here should be carefully used. Thus, in the case of defects with large height or depth, the assumption that the field near the defect can be expanded in series of only outgoing waves breaks down. In addition, in the case of defects with sharp corners one has to use in the field expansion a very large range of wave vectors, and thus the numerical algorithm might become impractical. Moreover, our study shows that the physical characteristics of the scattering process at the FF, namely, the distribution of the electromagnetic field and the spatial pattern of the emitted radiation, is markedly different from those of the scattering process at the SH, and therefore the surface generated SH could prove to be an invaluable noninvasive diagnosis tool in surface spectroscopy. In particular, we have demonstrated that the structure of the generated electromagnetic field at the SH is strongly dependent on the shape of the surface nanodefects and on the physical properties of the surface through the surface-profile function $\zeta(\mathbf{x}_\parallel)$ and the surface susceptibility $\hat{\chi}_s^{(2)}$, respectively. As a result, our study proves that the formalism introduced here has applicability to surface imaging or to surface physical chemistry, e.g., to measurements of physical quantities related to molecular adsorbates at interfaces or on metallic surfaces.

It is important to note, also, that our formalism can be easily extended to the case of more than one surface nanodefect or to a periodic distribution of such surface nanodefects. Thus, by extending our theoretical work to these more complex nanostructures would allow one not only to reach a deeper understanding of linear and nonlinear light interaction with nanopatterned metallic structure but also provide us with a powerful tool to design and investigate plasmonic nanodevices, such as light concentrators in deep-subwavelength spatial domains or optical nanoantennas.

ACKNOWLEDGMENTS

We are grateful to Jerry Dadap, George Flynn, and Mark Hybertsen for many useful discussions. The contribution to this work by N.C.P. was supported by NSF under Grant No. ECS-0523386, AFOSR under Grant No. FA9550-05-1-0428, and EPSRC under Grant No. EP/G030502/1, while that by L.C. and R.M.O. were sponsored by DOE through Grant No. DE-FG02-ER14104 and NSF through Grant No. DMR-08–06682.

APPENDIX: DIFFERENTIAL AND TOTAL SCATTERING CROSS SECTIONS AT THE FUNDAMENTAL FREQUENCY

The field distribution described by Eq. (1) contains two components that are of particular interest for an experimental investigation of scattering of SPPs by metallic nanostructures, namely, the far-field component radiated as an outward propagating *spherical wave*, in the region $x_3 \geq \zeta(\mathbf{x}_\parallel)$, and a *cylindrical SPP wave*, which represents the far-field component of the scattered SPP. The far-field distribution of the scattered light can be derived from Eq. (1) by using the stationary phase approximation[45] and is given by the expression

$$\mathbf{E}_{\mathrm{rad}}^{\uparrow}(\mathbf{x};\omega) = -\frac{i\omega}{2\pi c}\cos\theta_x \frac{e^{i\omega/cx}}{x}\left[\hat{\mathbf{e}}_p A_p\left(\hat{\mathbf{x}}_\parallel \frac{\omega}{c}\sin\theta_x\right) + \hat{\mathbf{e}}_s A_s\left(\hat{\mathbf{x}}_\parallel \frac{\omega}{c}\sin\theta_x\right)\right], \tag{A1}$$

whereas the far-field scattered SPP can be written as[43]

$$\mathbf{E}_{\mathrm{SPP}}^{\uparrow}(\mathbf{x};\omega) = \frac{c\alpha(\omega)}{\omega}\frac{e^{ik_\parallel(\omega)x_\parallel - \alpha_0(\omega)x_3 + i\pi/4}}{\sqrt{2\pi k_\parallel(\omega)x_\parallel}} \times \frac{i\hat{\mathbf{x}}_\parallel \alpha_0(\omega) - \hat{\mathbf{x}}_3 k_\parallel(\omega)}{\epsilon(\omega)+1} a_p(\hat{\mathbf{x}}_\parallel k_\parallel(\omega)). \tag{A2}$$

The unit vectors $\hat{\mathbf{e}}_s = (-\sin\phi_x, \cos\phi_x, 0)$ and $\hat{\mathbf{e}}_p = (\cos\theta_x\cos\phi_x, \cos\theta_x\sin\phi_x, -\sin\theta_x)$ in Eq. (A1) define the polarization direction of *s*- and *p*-polarized waves, respectively, whereas $\mathbf{x} = x(\sin\theta_x\cos\phi_x, \sin\theta_x\sin\phi_x, \cos\theta_x)$ is a vector that defines the direction of observation. Note that expression (A2) is equal to 2π times the residue of the integrand in Eq. (1) at the pole $q_\parallel = k_\parallel(\omega)$. Equations (A1) and (A2) can be used to calculate the amount of energy scattered into radiative modes (light) and surface plasmon waves. Thus, the power density radiated in the solid angle defined by angles θ_x and ϕ_x is $\frac{dP_{\mathrm{rad}}(\theta_x,\phi_x)}{d\Omega} = x^2 \Re\mathrm{e}\{S_{r,\mathrm{rad}}(\mathbf{x};\omega)\}$, whereas the power density emitted by the surface plasmon wave, in a direction defined by the angle ϕ_x, is $\frac{dP_{\mathrm{SPP}}(\phi_x)}{d\phi_x} = x_\parallel \Re\mathrm{e}\{S_{r,\mathrm{SPP}}(\mathbf{x};\omega)\}$. Here, $S_r(\mathbf{x};\omega)$ is the radial component of the Poynting vector. Moreover, the power density associated to the incident surface plasmon wave, per unit length, can be written as $\frac{dP_{\mathrm{inc}}}{dx_2} = \Re\mathrm{e}\{S_{1,\mathrm{inc}}(\mathbf{x};\omega)\}$, where the component $S_{1,\mathrm{inc}}(\mathbf{x};\omega)$ corresponds to the first term in the right-hand side of Eq. (1). Furthermore, these power densities can be used to define two differential scattering cross sections, $\sigma_{\mathrm{rad}}(\theta_x,\phi_x)$ and $\sigma_{\mathrm{SPP}}(\phi_x)$, which characterize the scattering of the incident surface plasmon wave into radiation and outgoing surface plasmons, respectively,

$$\Sigma_{\mathbf{rad}}(\theta_x,\phi_x) \equiv \frac{d\sigma_{\mathrm{rad}}}{d\Omega} = \frac{1}{P_{\mathrm{inc}}}\frac{dP_{\mathrm{rad}}(\theta_x,\phi_x)}{d\Omega}, \tag{A3a}$$

$$\Sigma_{\mathbf{SPP}}(\phi_x) \equiv \frac{d\sigma_{\mathrm{SPP}}}{d\phi_x} = \frac{1}{P_{\mathrm{inc}}}\frac{dP_{\mathrm{SPP}}(\phi_x)}{d\phi_x}. \tag{A3b}$$

Finally, from the differential scattering cross sections we can determine the total scattering cross sections, quantities that are given by the following expressions:

$$\sigma_{\mathrm{rad}} = \frac{1}{P_{\mathrm{inc}}}\int_0^{\pi/2} d\theta_x \sin\theta_x \int_{-\pi}^{\pi} d\phi_x x^2 \mathfrak{Re}\{S_{r,\mathrm{rad}}(\mathbf{x};\omega)\}, \tag{A4a}$$

$$\sigma_{\mathrm{SPP}} = \frac{1}{P_{\mathrm{inc}}}\int_0^{\infty} dx_3 \int_{-\pi}^{\pi} d\phi_x x_{\|} \mathfrak{Re}\{S_{r,\mathrm{SPP}}(\mathbf{x};\omega)\}. \tag{A4b}$$

Here, the incident power P_{inc} can be written as

$$P_{\mathrm{inc}} = \int_{-L/2}^{L/2} dx_2 \int_0^{\infty} dx_3 \mathfrak{Re}\{S_{1,\mathrm{inc}}(\mathbf{x};\omega)\}. \tag{A5}$$

*lc2233@columbia.edu

[1] H. Raether, *Surface Polaritons on Smooth and Rough Surfaces and on Gratings* (Springer-Verlag, Berlin, 1995).
[2] A. V. Zayats, I. I. Smolyaninov, and A. A. Maradudin, Phys. Rep. **408**, 131 (2005).
[3] T. F. Heinz, in *Nonlinear Surface Electromagnetic Phenomena*, edited by H. E. Panath and G. I. Stegeman (Elsevier, Amsterdam, 1991), p. 353.
[4] S. I. Bozhevolnyi and K. Pedersen, Surf. Sci. **377-379**, 384 (1997).
[5] U. Kreibig and M. Vollmer, *Optical Properties of Metal Clusters* (Springer-Verlag, Berlin, 1995).
[6] J. I. Dadap, J. Shan, and T. F. Heinz, J. Opt. Soc. Am. B **21**, 1328 (2004).
[7] K. B. Eisenthal, Chem. Rev. **106**, 1462 (2006).
[8] W. L. Barnes, A. Dereux, and T. W. Ebbesen, Nature (London) **424**, 824 (2003).
[9] T. W. Ebbesen, H. J. Lezec, H. F. Ghaemi, T. Thio, and P. A. Wolff, Nature (London) **391**, 667 (1998).
[10] S. I. Bozhevolnyi, J. Erland, K. Leosson, P. M. W. Skovgaard, and J. M. Hvam, Phys. Rev. Lett. **86**, 3008 (2001).
[11] S. K. Gray and T. Kupka, Phys. Rev. B **68**, 045415 (2003).
[12] W. Nomura, M. Ohtsu, and T. Yatsui, Appl. Phys. Lett. **86**, 181108 (2005).
[13] S. I. Bozhevolnyi, V. S. Volkov, E. Devaux, J. Y. Laluet, and T. W. Ebbesen, Nature (London) **440**, 508 (2006).
[14] X. P. Zhang, B. Q. Sun, R. H. Friend, H. C. Guo, D. Nau, and H. Giessen, Nano Lett. **6**, 651 (2006).
[15] J. Cesario, M. U. Gonzalez, S. Cheylan, W. L. Barnes, S. Enoch, and R. Quidant, Opt. Express **15**, 10533 (2007).
[16] R. M. Roth, N. C. Panoiu, M. M. Adams, J. I. Dadap, and R. M. Osgood, Opt. Lett. **32**, 3414 (2007).
[17] D. M. Schaadt, B. Feng, and E. T. Yu, Appl. Phys. Lett. **86**, 063106 (2005).
[18] J. Cole and N. J. Halas, Appl. Phys. Lett. **89**, 153120 (2006).
[19] N. C. Panoiu and R. M. Osgood, Opt. Lett. **32**, 2825 (2007).
[20] R. D. R. Bhat, N. C. Panoiu, S. R. J. Brueck, and R. M. Osgood, Opt. Express **16**, 4588 (2008).
[21] G. Boisde and A. Harmer, *Chemical and Biochemical Sensing with Optical Fibers and Waveguides* (Arthech House, Boston, 1996).
[22] J. L. West and N. J. Halas, Annu. Rev. Biomed. Eng. **5**, 285 (2003).
[23] R. M. Osgood, Jr. and D. J. Ehrlich, Opt. Lett. **7**, 385 (1982).
[24] C. J. Chen and R. M. Osgood, Phys. Rev. Lett. **50**, 1705 (1983).
[25] H. J. Simon, D. E. Mitchell, and J. G. Watson, Phys. Rev. Lett. **33**, 1531 (1974).
[26] A. V. Baranov, Y. S. Bobovich, and V. I. Petrov, Opt. Spektrosk. **58**, 578 (1985).
[27] C. K. Johnson and S. A. Soper, J. Phys. Chem. **93**, 7281 (1989).
[28] R. Antoine, P. F. Brevet, H. H. Girault, D. Bethell, and D. J. Schiffrin, Chem. Commun. (Cambridge) 1997, 1901.
[29] E. C. Hao, G. C. Schatz, R. C. Johnson, and J. T. Hupp, J. Chem. Phys. **117**, 5963 (2002).
[30] A. Bouhelier, M. Beversluis, A. Hartschuh, and L. Novotny, Phys. Rev. Lett. **90**, 013903 (2003).
[31] W. Fan, S. Zhang, N. C. Panoiu, A. Abdenour, S. Krishna, R. M. Osgood, K. J. Malloy, and S. R. J. Brueck, Nano Lett. **6**, 1027 (2006).
[32] L. Cao, N. C. Panoiu, and R. M. Osgood, Phys. Rev. B **75**, 205401 (2007).
[33] C. Hubert, L. Billot, P. M. Adam, R. Bachelot, P. Royer, J. Grand, D. Gindre, K. D. Dorkenoo, and A. Fort, Appl. Phys. Lett. **90**, 181105 (2007).
[34] N. C. Panoiu and R. M. Osgood, Nano Lett. **4**, 2427 (2004).
[35] J. I. Dadap, Phys. Rev. B **78**, 205322 (2008).
[36] S. M. Nie and S. R. Emery, Science **275**, 1102 (1997).
[37] K. Kneipp, Y. Wang, H. Kneipp, L. T. Perelman, I. Itzkan, R. R. Dasari, and M. S. Feld, Phys. Rev. Lett. **78**, 1667 (1997).
[38] C. L. Haynes and R. P. Van Duyne, J. Phys. Chem. B **107**, 7426 (2003).
[39] R. M. Roth, N. C. Panoiu, M. M. Adams, R. M. Osgood, C. C. Neacsu, and M. B. Raschke, Opt. Express **14**, 2921 (2006).
[40] A. Kubo, Y. S. Jung, H. K. Kim, and H. Petek, J. Phys. B **40**, S259 (2007).
[41] M. A. Ordal, L. L. Long, R. J. Bell, S. E. Bell, R. R. Bell, R. W. Alexander, and C. A. Ward, Appl. Opt. **22**, 1099 (1983); M. A. Ordal, R. J. Bell, R. W. Alexander, L. L. Long, and M. R. Querry, *ibid.* **24**, 4493 (1985).
[42] G. C. Brown, V. Celli, M. Haller, and A. Marvin, Surf. Sci. **136**, 381 (1984).
[43] A. V. Shchegrov, I. V. Novikov, and A. A. Maradudin, Phys.

Rev. Lett. **78**, 4269 (1997).
[44] J. A. Sanchez-Gil and A. A. Maradudin, Phys. Rev. B **60**, 8359 (1999).
[45] D. L. Mills, Phys. Rev. B **12**, 4036 (1975).
[46] A. A. Maradudin, in *Topics in Condensed Matter Physics*, edited by M. P. Das (Nova Science, New York, 1994), p. 33.
[47] N. Bloembergen, R. K. Chang, S. S. Jha, and C. H. Lee, Phys. Rev. **174**, 813 (1968).
[48] J. E. Sipe, V. C. Y. So, M. Fukui, and G. I. Stegeman, Phys. Rev. B **21**, 4389 (1980).
[49] J. E. Sipe, V. Mizrahi, and G. I. Stegeman, Phys. Rev. B **35**, 9091 (1987).
[50] G. S. Agarwal and S. S. Jha, Solid State Commun. **41**, 499 (1982).
[51] D. Krause, C. W. Teplin, and C. T. Rogers, J. Appl. Phys. **96**, 3626 (2004).
[52] J. D. Jackson, *Classical Electrodynamics*, 3rd ed. (Wiley & Sons, Hoboken, 1999).
[53] J. I. Dadap, J. Shan, K. B. Eisenthal, and T. F. Heinz, Phys. Rev. Lett. **83**, 4045 (1999).
[54] W. H. Press, S. A. Teukoisky, W. T. Vetterling, and B. P. Flannery, *Numerical Recipes in C* (Cambridge University Press, Cambridge, England, 1992).
[55] F. de Leon-Perez, G. Brucoli, F. J. Garcia-Vidal, and L. Martin-Moreno, New J. Phys. **10**, 105017 (2008).
[56] V. Kuzmiak and A. A. Maradudin, Phys. Rev. B **55**, 7427 (1997).
[57] T. Ito and K. Sakoda, Phys. Rev. B **64**, 045117 (2001).